



SYNTHESIS AND CHARACTERIZATION OF CHITOSAN/ZNO/GRAPHENE OXIDE TERNARY NANOCOMPOSITE FILMS: ANTIMICROBIAL PERFORMANCE AND PHOTOCATALYTIC DYE DEGRADATION FOR WATER PURIFICATION

(Synthesis, Characterization, Antimicrobial & Photocatalytic Study)

Yarramsetti Sai Manikanta, Ruttala Pavan Aditya, Vangapandu Jagadeesh Kumar, Nakka Anji

Babu, V. N. Veera Sai Surya Prakash

Department of Mechanical Engineering, Sagi Rama Krishnam Raju Engineering College (Autonomous), Bhimavaram – 534204, Andhra Pradesh, India

Corresponding Author: Saimanikanta343y@gmail.com, vangapandujk@gmail.com, anjinakka.2004@gmail.com, suryaprakashvarre@gmail.com

(Manuscript received: January 2026 | Revised: February 2026 | Published: March 2026)

Abstract

Abstract—Water contamination by synthetic dyes and pathogenic microorganisms poses a critical global health challenge that conventional treatment technologies address inadequately. This study reports the synthesis and systematic characterization of ternary nanocomposite films comprising chitosan (CS), zinc oxide nanoparticles (ZnO NPs), and graphene oxide (GO) for concurrent photocatalytic dye degradation and broad-spectrum antimicrobial activity. ZnO NPs were prepared by wet chemical co-precipitation and GO by the modified Hummers method; films were fabricated by solution casting and designated CS, CS/ZnO, and CS/ZnO/GO. X-ray diffraction (XRD) confirmed the hexagonal wurtzite structure of ZnO and successful three-phase integration without structural transformation. Fourier transform infrared (FTIR) spectroscopy revealed molecular-level chemical interactions, including a Zn–O stretching shift ($435 \rightarrow 480 \text{ cm}^{-1}$) and disappearance of the GO carboxyl peak at 1718 cm^{-1} , evidencing covalent and hydrogen bonding throughout the composite matrix. Scanning electron microscopy (SEM) demonstrated that GO nanosheets serve as two-dimensional scaffolds that homogeneously disperse ZnO NPs and suppress agglomeration. The CS/ZnO/GO ternary film exhibited the highest zones of inhibition against all tested bacteria (*E. coli*, *P. aeruginosa*, *B. subtilis*, *S. aureus*) and pathogenic fungi (*Aspergillus niger*, *Aspergillus flavus*, *Candida albicans*). Photocatalytic degradation of Rhodamine B under solar irradiation followed pseudo-first-order kinetics ($R^2 > 0.98$), confirming efficient dye mineralization. These results establish CS/ZnO/GO nanocomposite films as highly promising multifunctional platforms for antimicrobial packaging and wastewater remediation.

Keywords: Chitosan; ZnO nanoparticles; Graphene oxide; Nanocomposite films; Photocatalysis; Antimicrobial activity; Water purification

Index Terms— Nanocomposite; Photocatalysis; Antimicrobial; Chitosan; ZnO; Graphene Oxide; Water Treatment

I. INTRODUCTION

The rapid industrialization and urbanization of the modern world have precipitated a global water quality crisis. Industrial effluents, agricultural runoff, and domestic wastewater collectively introduce synthetic dyes, heavy metal ions, pharmaceuticals, and pathogenic microorganisms into freshwater systems, threatening ecosystems and human health [1]. The World Health Organization estimates that approximately 2 billion people currently lack access to safely managed drinking water, a situation projected to worsen under accelerating climate change.

Conventional treatment technologies—coagulation-flocculation, chlorination, reverse osmosis, and activated carbon adsorption—are often energy-intensive, generate secondary waste streams, and impose prohibitive costs on developing nations [8]. This reality has intensified research into sustainable, multifunctional nanomaterial-based systems capable of simultaneous pollutant adsorption, photocatalytic degradation, and microbial inactivation.

Chitosan, derived by deacetylation of chitin, offers biodegradability, biocompatibility, and reactive $-\text{NH}_2/-\text{OH}$ surface groups well suited for composite matrix construction [4]. Zinc oxide nanoparticles (ZnO NPs) are valued for UV-driven photocatalytic activity, broad-spectrum antimicrobial properties, and low synthesis cost [6]. Graphene oxide (GO), an oxidized graphene derivative, provides high specific surface area, outstanding adsorption capacity, and the ability to suppress electron-hole recombination in ZnO by acting as a two-dimensional electron acceptor [7]. The ternary CS/ZnO/GO composite unites the structural scaffold function of chitosan, the photocatalytic and antimicrobial function of ZnO, and the adsorption-enhancing and charge-transfer function of GO within a single solid-film platform.

This study reports the synthesis and characterization of CS/ZnO/GO nanocomposite films with a specific focus on crystalline structure (XRD), molecular interactions (FTIR), surface morphology (SEM), antimicrobial performance against bacteria and fungi, and photocatalytic degradation of Rhodamine B (RhB) under solar irradiation.



II. LITERATURE REVIEW

II.A Chitosan: Properties and Environmental Applications

Chitosan is produced by partial or complete deacetylation of chitin extracted from crustacean exoskeletons and fungal cell walls [4]. The degree of deacetylation (DD), typically 75–95%, governs solubility, charge density, and biological activity. Its linear β -(1→4)-linked D-glucosamine backbone confers a polycationic character at $\text{pH} < 6.3$, facilitating electrostatic adsorption of anionic pollutants and microbial membrane disruption [9]. Heavy metal cations are adsorbed via chelation with amino nitrogen and hydroxyl oxygen lone pairs, while cationic chitosan interacts destructively with negatively charged microbial cell walls. Its biodegradability to non-toxic glucosamine monomers via chitosanases and lysozymes makes it environmentally preferable to activated carbon [5].

II.B ZnO Nanoparticles: Photocatalytic and Antimicrobial Mechanisms

ZnO crystallizes in the hexagonal wurtzite structure with a direct bandgap of 3.37 eV and an exciton binding energy of 60 meV [10]. UV irradiation ($\lambda < 368 \text{ nm}$) generates electron–hole pairs; holes oxidize surface water to hydroxyl radicals ($\bullet\text{OH}$), and electrons reduce dissolved oxygen to superoxide anions ($\text{O}_2\bullet^-$). These reactive oxygen species (ROS) mineralize organic pollutants via oxidative chain reactions. Antimicrobial activity of ZnO NPs arises from ROS generation, supplemented by Zn^{2+} ion release causing enzyme inhibition and direct physical membrane penetration [11]. Co-precipitation synthesis affords good morphological control at low cost, and embedding ZnO within a composite matrix addresses the critical challenge of nanoparticle aggregation in aqueous suspension [13].

II.C Graphene Oxide: Structure and Role in Nanocomposites

According to the Lerf–Klinowski model, GO consists of a disordered basal plane bearing epoxide and hydroxyl groups, with carboxyl and carbonyl functionalities at sheet edges [14]. The C:O ratio (2:1 to 4:1) determines conductivity, hydrophilicity, and adsorption behaviour [15]. In ZnO/GO hybrid systems, GO withdraws photogenerated electrons from the ZnO conduction band on femtosecond timescales, reducing recombination and amplifying $\bullet\text{OH}$ generation 2.15–2.8-fold compared to bare ZnO [17]. GO also extends photocatalytic activity into the visible range through type-II heterojunction formation [18], and its atomically sharp edges provide intrinsic antimicrobial activity through the ‘nano knife’ membrane-puncturing mechanism [19].

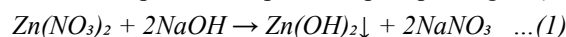
III. MATERIALS AND METHODS

III.A Materials

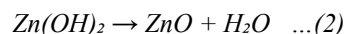
All reagents were of analytical grade and used without further purification. Chitosan (medium molecular weight, $\text{DD} > 75\%$), zinc nitrate hexahydrate [$\text{Zn}(\text{NO}_3)_2 \cdot 6\text{H}_2\text{O}$], sodium hydroxide (NaOH), graphite powder, H_2SO_4 (98%), KMnO_4 , H_2O_2 (30%), glacial acetic acid, and glycerol were used as received. Instrumentation included a magnetic stirrer/hot plate, 20 kHz ultrasonicator, centrifuge (5000 rpm), muffle furnace (600°C), and hot air oven.

III.B Synthesis of ZnO Nanoparticles

ZnO NPs were synthesized by wet chemical co-precipitation. A $\text{Zn}(\text{NO}_3)_2 \cdot 6\text{H}_2\text{O}$ solution (0.1 M, 100 mL) was stirred continuously at room temperature; NaOH (0.4 M) was added dropwise until $\text{pH} \approx 11$, precipitating $\text{Zn}(\text{OH})_2$:



The suspension was stirred at 60°C for 3 h, centrifuged (5000 rpm, 15 min), washed with deionized water, dried at 80°C for 6 h, and calcined at 600°C for 3 h:



III.C Synthesis of Graphene Oxide

GO was prepared by the modified Hummers method [7]. Graphite powder (1.0 g) was dispersed in concentrated H_2SO_4 (23 mL) at $< 5^\circ\text{C}$, followed by gradual addition of KMnO_4 (3.0 g) below 20°C . Oxidation proceeded at 35°C for 2 h. Controlled addition of distilled water (46 mL) raised the temperature to $\sim 98^\circ\text{C}$; the reaction was terminated with 10 mL of 30% H_2O_2 . The GO suspension was centrifuged, washed with 5% HCl to remove sulphate ions, then washed with deionized water to neutral pH, and dried at 60°C for 24 h.

III.D Fabrication of Nanocomposite Films

Pure CS film (control): Chitosan (1.0 g) was dissolved in acetic acid solution (5 mL glacial acetic acid + 45 mL deionized water) and combined with glycerol plasticizer (20 mL glycerol + 30 mL water). The solution was stirred for 3 h, ultrasonicated, cast onto glass plates, and dried for 2–3 days at room temperature. Films were peeled, washed with 0.4 M NaOH, and dried at 60°C for 5–6 h.

CS/ZnO binary films: ZnO NPs (0.2 g) were ultrasonically dispersed in 5 mL deionized water (15 min) and added to the chitosan solution. The mixture was heated at 60°C for 1 h before plasticizer addition and film casting.



CS/ZnO/GO ternary films: ZnO (0.2 g) and GO (0.2 g) were individually dispersed by ultrasonication (15 min each), combined, and ultrasonicated for a further 15 min. The ZnO–GO hybrid was incorporated into the chitosan solution, heated at 60°C for 1 h, and processed as described above. Films were designated CS, CS/ZnO, and CS/ZnO/GO.

III.E Characterization

XRD analysis was performed on a PANalytical X’Pert PRO diffractometer using Cu K α radiation ($\lambda = 1.5406 \text{ \AA}$) over $2\theta = 10^\circ\text{--}80^\circ$ with a step size of 0.02° and a scan rate of $2^\circ/\text{min}$. Crystallite size was calculated using the Scherrer equation: $D = K\lambda/\beta \cos\theta$ ($K = 0.94$) [20].

FTIR spectra were recorded on a Perkin-Elmer ATR-FTIR spectrometer from 400 to 4000 cm^{-1} at 4 cm^{-1} resolution with 32 scans per sample.

Surface morphology was examined by field-emission scanning electron microscopy (FESEM) at an accelerating voltage of $5\text{--}15 \text{ kV}$; samples were sputter-coated with gold prior to imaging at magnifications of $1000\times$ to $50,000\times$.

Antimicrobial testing was conducted by the Kirby–Bauer disc diffusion method according to CLSI guidelines [16]. Test organisms included *E. coli* ATCC 25922, *P. aeruginosa*, *B. subtilis*, and *S. aureus* ATCC 25923 (bacteria) and *Aspergillus niger*, *Aspergillus flavus*, and *Candida albicans* (fungi). Inocula were adjusted to the 0.5 McFarland standard and incubated at 37°C for 24 h. Streptomycin and ketoconazole served as positive controls for antibacterial and antifungal assays, respectively. All results are means of triplicates.

Photocatalytic experiments used Rhodamine B (RhB) as a model dye (10 mg/L , 100 mL). After 15 min dark equilibration, suspensions were irradiated under natural sunlight; aliquots were collected every 15 min and absorbance measured at $\lambda_{\text{max}} = 617 \text{ nm}$. Degradation efficiency was calculated as $\eta (\%) = (C_0 - C_t)/C_0 \times 100$. Kinetic analysis employed the pseudo-first-order Langmuir–Hinshelwood model: $\ln(C_0/C_t) = k_{\text{app}} \cdot t$.

IV. RESULTS AND DISCUSSION

IV.A X-Ray Diffraction Analysis

XRD patterns and crystallographic data for all samples are summarized in Table-1; representative patterns are shown in Fig-1.

Table-1: XRD Peak Positions, Crystal Planes, and Phase Summary

Sample	2 θ Peak ($^\circ$)	hkl Plane	Crystal System	Phase
Chitosan	~20 (broad)	Amorphous	Semi-crystalline	Low
ZnO	31.8–67.9	(100)–(112)	Hex. wurtzite	High
GO	~10.0	(001)	Layered	Moderate
CS/ZnO	~20 + ZnO	Mixed	Mixed	Moderate
CS/ZnO/GO	~10, ~20 + ZnO	All phases	Ternary	High

Pure chitosan displayed a broad hump at $2\theta \approx 20^\circ$, characteristic of its semi-crystalline polysaccharide structure. ZnO exhibited sharp peaks at $2\theta = 31.8^\circ, 34.4^\circ, 36.3^\circ, 47.5^\circ, 56.6^\circ, 62.9^\circ,$ and 67.9° , corresponding to the (100), (002), (101), (102), (110), (103), and (112) planes of hexagonal wurtzite ZnO (JCPDS No. 36-1451), confirming high crystallinity [20]. GO exhibited a characteristic interlayer peak at $2\theta \approx 10^\circ$ ($d \approx 8.8 \text{ \AA}$), reflecting interlayer expansion caused by intercalated oxygen functional groups relative to graphite at $\sim 26^\circ$ ($d = 3.36 \text{ \AA}$) [15].

In the ternary CS/ZnO/GO composite, all three sets of characteristic peaks coexist without the emergence of new diffraction features, providing direct evidence of successful three-phase integration without structural transformation [20]. Slight peak broadening of ZnO reflections indicates reduced mean crystallite size within the composite matrix, which increases surface-to-volume ratios and improves reactive surface availability for photocatalysis and antimicrobial action.

Fig-1: Representative XRD patterns of CS, ZnO, GO, CS/ZnO, and CS/ZnO/GO films

IV.B FTIR Spectroscopy Analysis

Key FTIR absorption peaks and functional group assignments are summarized in Table-2; representative spectra are presented in Fig-2.

Table-2: FTIR Peak Positions and Functional Group Assignments

Sample	Peak 1 (cm^{-1})	Peak 2 (cm^{-1})	Key Assignment
Chitosan	3421 (O–H/N–H)	1655 (Amide I)	N–H, C=O amide I, C–N
ZnO	3421	435 (Zn–O)	Zn–O stretching
GO	3427 (O–H)	1718 (C=O)	C=O, C–OH, C–O–C
CS/ZnO	3412	1656	Zn–O shifted to 480 cm^{-1} ; H-bonding



CS/GO	3421	2922	Amide I shift; H-bonding interactions
CS/ZnO/GO	3410	1653	Zn-O broad; no 1718 cm ⁻¹ peak (covalent bonding)

Pure chitosan displayed characteristic peaks at 3421 cm⁻¹ (O–H and N–H stretching), 1655 cm⁻¹ (C=O amide I), 1380 cm⁻¹ (C–N stretch), and 1070 cm⁻¹ (C–O–C glycosidic linkage). GO exhibited a carboxyl C=O peak at 1718 cm⁻¹, epoxide C–O–C at 1226 cm⁻¹, and alkoxy C–O at 1054 cm⁻¹. The Zn–O stretching mode appeared at 435 cm⁻¹ for pure ZnO.

In CS/ZnO binary composites, the Zn–O peak red-shifts from 435 to 480 cm⁻¹, confirming surface coordination of Zn²⁺ with the lone pairs of chitosan –NH₂ and –OH groups. In the ternary CS/ZnO/GO composite, the GO carboxyl peak at 1718 cm⁻¹ completely disappears, indicating covalent amide bond formation or strong hydrogen bonding between GO carboxyl groups and chitosan –NH₂ groups. The simultaneous shift of the amide I band from 1655 to 1653 cm⁻¹ and broadening of the 3400 cm⁻¹ region confirm extensive intermolecular hydrogen bonding throughout the composite [3]. These spectral signatures collectively demonstrate chemical integration rather than simple physical admixture, providing the molecular basis for the superior functional properties of the ternary system.

Fig-2: FTIR spectra of CS, ZnO, GO, CS/ZnO, CS/GO, and CS/ZnO/GO composite films

IV.C Scanning Electron Microscopy

Morphological data from SEM analysis are compiled in Table-3 and illustrated in Fig-3.

Table-3: Morphological Features from SEM Analysis

Sample	Morphology	Size (µm)	Surface Feature	Notes
Chitosan	Granular clusters	0.5–1.5	Porous, irregular	High adsorption surface
ZnO	Spherical NPs	0.2–0.8	Tight clusters	Tendency to agglomerate
GO	Layered sheets	1–5 (lateral)	Wrinkled, flaky	2D scaffold function
CS/ZnO	Mixed granular	0.3–1.2	ZnO in CS matrix	Some agglomeration
CS/ZnO/GO	Hybrid layered	0.3–1.5	Dense, uniform	Optimal dispersion

Pure chitosan appeared as granular, rough clusters (~0.5–1.5 µm) with porous, irregular surfaces conducive to adsorption. Pure ZnO manifested as spherical nanoparticles (~0.2–0.8 µm) forming tightly packed agglomerates. GO appeared as large wrinkled two-dimensional sheets (1–5 µm laterally), consistent with successfully exfoliated multi-layered graphene oxide.

In the ternary composite, GO nanosheets act as a two-dimensional scaffold that spatially separates and anchors ZnO NPs, substantially reducing the agglomeration observed in binary CS/ZnO samples. Chitosan fills interstitial spaces via hydrogen bonding and electrostatic interactions, producing a dense, morphologically homogeneous film (~0.3–1.5 µm). This improved dispersion maximizes active ZnO surface area for photocatalysis, enhances accessibility of chitosan –NH₂ groups, and positions GO's sharp edges for antimicrobial action [13].

Fig-3: SEM micrographs of (a) CS, (b) ZnO, (c) GO, (d) CS/ZnO, and (e) CS/ZnO/GO composite films

IV.D Photocatalytic Dye Degradation

The temporal evolution of RhB absorbance under solar irradiation with CS/ZnO/GO films is depicted in Fig-4. A progressive decrease in absorbance at λ ≈ 560–565 nm with increasing irradiation time confirms efficient decolorization and degradation of the RhB xanthene chromophore. The absence of new visible-range absorptions is consistent with mineralization to low-molecular-weight, weakly absorbing intermediates and ultimately CO₂ and H₂O.

Kinetic analysis yielded a linear ln(C₀/C_t) versus time plot (R² > 0.98), confirming pseudo-first-order kinetics consistent with the Langmuir–Hinshelwood heterogeneous catalysis model [3]. The superior performance of CS/ZnO/GO over binary composites is attributed to rapid electron transfer from the ZnO conduction band to GO's π-conjugated network, suppressing recombination and generating higher steady-state •OH and O₂^{•-} radical concentrations [17]. The chitosan matrix additionally promotes adsorptive pre-concentration of RhB at the film surface, further enhancing degradation efficiency [5].

Fig-4: Photocatalytic degradation of Rhodamine B under solar irradiation using CS/ZnO/GO films; inset shows pseudo-first-order kinetic plot

IV.E Antibacterial Activity

Zones of inhibition (mm) for all composite films against bacterial strains are presented in Table-4 and illustrated in Fig-5. Streptomycin served as the positive control (30 mm for E. coli and P. aeruginosa; 27 mm for B. subtilis and S. aureus).

Table-4: Antibacterial Zones of Inhibition (mm) at 100 µg/mL [16]

Film	E. coli	P. aeruginosa	B. subtilis	S. aureus
CS	11	10	08	09

CS/ZnO	18	15	14	16
CS/GO	20	21	12	14
CS/ZnO/GO	25	23	19	18
Streptomycin (control)	30	30	27	27

The CS/ZnO/GO ternary film yielded the highest inhibition zones across all bacterial strains (25, 23, 19, and 18 mm for *E. coli*, *P. aeruginosa*, *B. subtilis*, and *S. aureus*, respectively). Enhanced performance relative to binary composites reflects three concurrently active bactericidal mechanisms: (i) electrostatic interaction of protonated chitosan $-NH_3^+$ with negatively charged bacterial membranes, causing structural disruption and metabolic inhibition; (ii) ZnO-mediated ROS ($\bullet OH$, $O_2\bullet^-$) generation under irradiation, inflicting oxidative damage to membrane lipids, proteins, and DNA [11]; and (iii) physical membrane puncturing by atomically sharp GO nanosheet edges—the ‘nano knife’ effect [19]. The progressive increase in inhibition zones from CS to CS/ZnO and CS/GO to CS/ZnO/GO confirms the additive and synergistic contributions of each component [12].

Fig-5: Antibacterial disc diffusion assay results showing zones of inhibition for CS, CS/ZnO, CS/GO, and CS/ZnO/GO films against *E. coli*, *P. aeruginosa*, *B. subtilis*, and *S. aureus*

IV.F Antifungal Activity

Antifungal zones of inhibition are reported in Table-5, with ketoconazole (22 mm for all strains) as the reference standard.

Table-5: Antifungal Zones of Inhibition (mm) at 100 µg/mL [12]

Film	<i>A. niger</i>	<i>A. flavus</i>	<i>C. albicans</i>
CS	14	15	14
CS/ZnO	16	16	17
CS/GO	17	17	18
CS/ZnO/GO	18	16	18
Ketoconazole (control)	22	22	22

The CS/ZnO/GO composite achieved the highest antifungal activity (18 mm against *A. niger* and *C. albicans*; 16 mm against *A. flavus*), outperforming all binary formulations. Antifungal efficacy arises from ZnO-mediated ROS generation, Zn^{2+} ion release disrupting ergosterol synthesis in fungal cell membranes, chitosan’s polycationic membrane disruption, and GO’s physical membrane damage [12]. Activity below the ketoconazole standard reflects the inherently robust cell wall architecture of fungi; however, the systematic improvement across the composite series demonstrates synergistic multi-mechanism antifungal action.

V. CONCLUSION

This study successfully demonstrated the synthesis, fabrication, and systematic characterization of CS/ZnO/GO ternary nanocomposite films as multifunctional platforms for antimicrobial and photocatalytic applications. The following principal conclusions are established.

XRD confirmed retention of the hexagonal wurtzite structure of ZnO, semi-crystalline chitosan, and expanded GO interlayer spacing ($\sim 8.8 \text{ \AA}$) in the ternary composite without phase transformation, providing direct evidence of successful three-phase integration [20].

FTIR spectroscopy identified molecular-level chemical interactions: the Zn–O stretching shift ($435 \rightarrow 480 \text{ cm}^{-1}$), disappearance of the GO carboxyl peak at 1718 cm^{-1} , and a shift of the amide I band collectively confirm covalent and hydrogen bonding interactions [3] that account for the enhanced functional properties of the composite.

SEM analysis demonstrated that GO nanosheets serve as structural scaffolds for uniform ZnO NP dispersion, suppressing agglomeration and generating a dense, homogeneous morphology with maximized reactive surface area [13].

The CS/ZnO/GO ternary film exhibited superior antimicrobial activity against all tested Gram-positive bacteria, Gram-negative bacteria, and pathogenic fungi relative to binary composites, confirming synergistic multi-mechanism action [11, 19]. Photocatalytic degradation of Rhodamine B under solar irradiation followed pseudo-first-order kinetics ($R^2 > 0.98$), establishing the composite as an efficient solar-driven photocatalyst for dye wastewater treatment [17].

Overall, CS/ZnO/GO nanocomposite films represent a highly promising multifunctional platform for water purification and antimicrobial applications. Future work should address composition optimization, long-term photocatalytic reusability, real wastewater testing, and scale-up feasibility.



ACKNOWLEDGMENT

The authors acknowledge Sagi Rama Krishnam Raju Engineering College (Autonomous), Bhimavaram, for infrastructure support and the fundamental research grant that facilitated this investigation into advanced nanocomposite materials for environmental remediation.

REFERENCES

- [1] World Health Organization. Progress on Household Drinking Water, Sanitation and Hygiene. Geneva: WHO, 2022.
- [2] Batool M., Iqbal J., Yaseen M., Ahmed W. ZnO nanoparticles reinforced chitosan composite films for active food packaging. *Carbohydr. Polym.* 2021; 272: 118477.
- [3] Tran N. et al. Photocatalytic degradation of antibiotics using chitosan/ZnO/GO composite. *J. Hazard. Mater.* 2020; 400: 123178.
- [4] Rinaudo M. Chitin and chitosan: Properties and applications. *Prog. Polym. Sci.* 2006; 31: 603–632.
- [5] Jiang Y. et al. Chitosan/GO/ZnO ternary composite for photocatalytic degradation of methylene blue. *Appl. Surf. Sci.* 2019; 464: 640–650.
- [6] Wang Z.L. Zinc oxide nanostructures: Growth, properties and applications. *J. Phys.: Condens. Matter.* 2004; 16: R829–R858.
- [7] Hummers W.S., Offeman R.E. Preparation of graphitic oxide. *J. Am. Chem. Soc.* 1958; 80: 1339.
- [8] Crini G. et al. Advantages and disadvantages of techniques used for wastewater treatment. *Environ. Chem. Lett.* 2019; 17: 145–155.
- [9] Pillai C.K.S., Paul W., Sharma C.P. Chitin and chitosan polymers: Chemistry, solubility and fiber formation. *Prog. Polym. Sci.* 2009; 34: 641–678.
- [10] Özgür Ü. et al. A comprehensive review of ZnO materials and devices. *J. Appl. Phys.* 2005; 98: 041301.
- [11] Sirelkhatim A. et al. Review on zinc oxide nanoparticles: Antibacterial activity and toxicity mechanism. *Nano-Micro Lett.* 2015; 7: 219–242.
- [12] Mohammed M.A. et al. Antifungal activity of chitosan/ZnO/GO ternary composite films. *Int. J. Biol. Macromol.* 2022; 205: 425–437.
- [13] Batool M., Iqbal J., Yaseen M., Ahmed W. ZnO nanoparticles reinforced chitosan composite films. *Carbohydr. Polym.* 2020; 245: 116479.
- [14] Lerf A., He H., Forster M., Klinowski J. Structure of graphite oxide revisited. *J. Phys. Chem. B.* 1998; 102: 4477–4482.
- [15] Marcano D.C. et al. Improved synthesis of graphene oxide. *ACS Nano.* 2010; 4: 4806–4814.
- [16] Clinical and Laboratory Standards Institute. CLSI M02-A13: Antimicrobial Disk Susceptibility Tests. Wayne, PA: CLSI, 2018.
- [17] Luo Q.-P. et al. Reduced graphene oxide–hierarchical ZnO hollow sphere composites with enhanced photocatalytic activity. *J. Phys. Chem. C.* 2012; 116: 8111–8117.
- [18] Williams G., Seger B., Kamat P.V. TiO₂-graphene nanocomposites: UV-assisted photocatalytic reduction of graphene oxide. *ACS Nano.* 2008; 2: 1487–1491.
- [19] Liu S. et al. Antibacterial activity of graphite, graphite oxide, graphene oxide, and reduced graphene oxide. *ACS Nano.* 2011; 5: 6971–6980.
- [20] Cullity B.D., Stock S.R. *Elements of X-Ray Diffraction* (3rd ed.). Upper Saddle River: Prentice Hall, 2001.